Wiley Online Library
Early View publication on www.wileyonlinelibrary.com
(issue and page numbers not yet assigned;
citable using Digital Object Identifier – DOI)

J. Biophotonics 1–11 (2016) / **DOI** 10.1002/jbio.201600173

Journal of BIOPHOTONICS

FULL ARTICLE

# Distinction between breast cancer cell subtypes using third harmonic generation microscopy

*Evangelia Gavgiotaki*[1, 2], *George Filippidis*[*, 1], *Haris Markomanolaki*[2], *George Kenanakis*[1], *Sofia Agelaki*[2], *Vassilis Georgoulias*[2], *and Irene Athanassakis*[*, 3]

[1] Institute of Electronic Structure and Laser, Foundation for Research and Technology, Heraklion 71110, Crete, Greece
[2] Medical School, University of Crete, Heraklion 71003, Crete, Greece
[3] Department of Biology, University of Crete, Heraklion 71409, Crete, Greece

Received 8 June 2016, revised 10 September 2016, accepted 30 September 2016
Published online 19 October 2016

**Key words:** Third Harmonic Generation, nonlinear imaging, microscopy, breast cancer cells, lipid droplets, quantification, FTIR spectroscopy, linkage

Third Harmonic Generation (THG) microscopy as a non-invasive, label free imaging methodology, allows linkage of lipid profiles with various breast cancer cells. The collected THG signal arise mostly from the lipid droplets and the membrane lipid bilayer. Quantification of THG signal can accurately distinguish HER2-positive cells. Further analysis using Fourier transform infrared (FTIR) spectra reveals cancer-specific profiles, correlating lipid raft-corresponding spectra to THG signal, associating thus THG to chemical information.

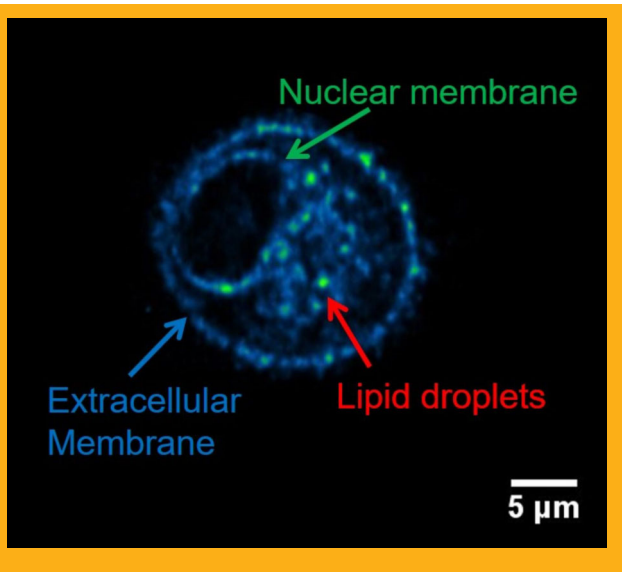


THG imaging of a cancer cell.

## 1. Introduction

Nonlinear imaging microscopy modalities [Two Photon excitation Fluorescence (TPEF), Second Harmonic Generation (SHG), Third Harmonic Generation (THG)] are well-established techniques for biological applications [1–9]. The investigation of *in vivo* cellular and sub-cellular activities, by means of these non-destructive techniques, can provide valuable information related to fundamental biological problems, leading to the development of innovative methodologies for the early diagnosis and treatment of various diseases, including cancer.

THG is a coherent nonlinear scattering phenomenon and is sensitive to local differences in third-order nonlinear susceptibility $\chi^{(3)}$, refractive index and

* Corresponding authors: e-mail: athan@biology.uoc.gr, filip@iesl.forth.gr


© 2016 WILEY-VCH Verlag GmbH & Co. KGaA, Weinheim

dispersion. Under tight focusing conditions, the extent of THG signal increases dramatically when the beam focus spans an interface between two optically different materials. In THG microscopy, the contrast arises from interfaces and optical heterogeneities of size comparable to the beam focus. No THG signal is collected when the laser beam is focused inside a homogeneous, normally dispersive medium [10, 11].

THG microscopy provides high-contrast images of lipid droplets (LDs), which can be detected with high specificity in a variety of cells [12]. Previous studies have shown that THG imaging can distinguish between activated and non-activated microglia cells through increased signal detection from LDs [8]. Moreover, THG imaging renders three-dimensional (3D) spatial resolution of the samples and can be used to study LDs in a complex environment, such as intact cells and tissues [12].

Lipid droplets are lipid rich cytoplasmic organelles formed by a neutral lipid core surrounded by a monolayer of phospholipids hosting a diverse array of associated proteins. The increased number of LDs has been correlated to pathological conditions including inflammatory, infectious diseases and tumorigenic processes [13–16].

Complementary information can be provided by Fourier transform infrared (FTIR) spectroscopy, which is used for the detection and classification of various types of molecules. FTIR analysis, qualitatively and quantitatively characterizes various biomolecular features of cancer cells and tissues [17–19].

The present study concentrated on breast cancer cell lines. Breast cancer is one of the most frequently diagnosed types of cancer and the leading cause of cancer death in women [20]. Using representative cell lines, the aim of the present study was to evaluate whether THG imaging could detect qualitative and quantitative differences between the different subtypes of breast cancer and control cells and relate those to FTIR spectra. The obtained results suggest that, THG microscopy could be a new label free diagnostic tool for classification of breast cancer cells, while correlating to specific FTIR spectra, associating thus THG signal to chemical information.

## 2. Experimental

### 2.1 Cell lines and culture condition

Luminal (T47D, MCF7), Her2+ (BT474, SKBR3) and triple negative (MDA-MB231, Hs578t) human breast cancer cell lines were purchased from ATCC (Rockville, Maryland, USA) and maintained at 37 °C in a humidified atmosphere of 5% $CO_2$ in air. MDA-MB231 and Hs578t cell lines were cultured in DMEM medium (GIBCO 61965-026, Grand Island, NY) supplemented with 10% FBS (GIBCO-BRL) and 50 mg/mL penicillin/streptomycin (GIBCO-BRL). For MCF7 and T47D cell cultures, the above medium was supplemented with 16 ng/mL and 11 ng/mL insulin, respectively. SKBR3 cells were cultured in McCoy's medium (GIBCO-BRL) supplemented with 10% FBS and 50 mg/mL penicillin/streptomycin. BT474 cells were cultured in DMEM/Ham's F12 medium (GIBCO-BRL) supplemented with 10% FBS, 2 mM L-glutamine (GIBCO-BRL), 1 mM sodium pyruvate (GIBCO-BRL) and 50 mg/mL penicillin/streptomycin. For sub-cultivation cells were detached using 0.25% trypsin and 5 mmol/L EDTA (GIBCO-BRL). All experiments were carried out during the logarithmic growth phase. The passage number remained stable for all cell lines. Non-tumorigenic MCF10a human breast cells were cultured in DMEM/Ham's F12 medium supplemented with 5% horse serum (GIBCO), 50 mg/mL penicillin/streptomycin, 100 µL EGF, 250 µl hydrocortisone, 50 µl cholera toxin, and 16 ng/mL insulin.

Peripheral blood mononuclear cells (PBMCs) were isolated from healthy blood donors ($n = 3$). Peripheral blood (10 ml) was placed on a Ficoll-Hypaque density gradient ($d = 1{,}077$ g/mol) and upon centrifugation at 1800 rpm for 30 minutes, PBMCs were collected from the interface and washed three times with PBS by centrifugation at 1500 rpm for 10 minutes.

For lipid droplet staining, cells were fixed with PFA 4% (Sigma-Aldrich Co., MO, USA, 158127), permeabilized with PBS-Triton X-100 0.025% (Sigma, X100) and stained with Nile Red (10 µg/ml, Sigma, N3013).

### 2.2 Experimental setup

The experimental apparatus consisted of an Yb-based femtosecond (fs) laser oscillator emitting at a central wavelength of 1028 nm (Amplitude Systemes, *t*-pulse, 200 fs, 50 MHz, 1 Watt) combined with a modified upright microscope (Nikon Eclipse ME600D) as previously described [4, 8] (Figure 1 supplementary material).

Briefly, adjustable neutral density filters (New Focus) were utilized to control the power at the sample plane. The laser beam passes through mirrors and directed on a pair of galvanometric mirrors (Cambridge Technologies). Galvanometric mirrors were employed in order to perform the fast raster scanning in the selected xy plane of the sample. The focal plane was adjusted by using a motorized translation stage (Standa Ltd. 1 µm minimum step). A telescope system was used to expand the beam dia-

© 2016 WILEY-VCH Verlag GmbH & Co. KGaA, Weinheim

meter in order to fill the back aperture of the objective lens. The beam was tightly focused on the sample by employing a high Numerical Aperture (NA) objective lens (Carl Zeiss, C-Achroplan 32×, NA 0.85, water immersion). By employing diffraction limited focused fs laser beams, nonlinear phenomena at the sample plane of the biological specimens could be created. Using such setup it was possible to collect simultaneously two different nonlinear signals, one in the transmission (THG) and the other in the reflection mode (TPEF), providing thus the opportunity to perform co-localization measurements. On the transmission mode THG signal was recorded, after passing through a condenser lens (Carl Zeiss, PlanNeofluar, 40×, 0.75 NA, air immersion) and a coloured glass filter (U 340-Hoya), from a photo multiplier tube (PMT, Hamamatsu). On the reflection mode, TPEF signals were detected by using a second PMT (Hamamatsu). An appropriate short pass filter (SPF 700 nm, CVI) was employed in the case of TPEF measurements (Nile Red staining) along with a bandpass filter (640 nm/40 nm, Chroma). A computer controlled both scanning and data acquisition procedures. The samples were placed between two very thin round glasses (70 μm, Marienfeld) separated by a copper spacer (100 μm thickness) to avoid damage the cells. A CCD camera (PixeLINK) was used for the optical observation of our specimens.

The alignment and the optimization of the system was performed using the collection of the maximum THG signals from the air/glass and glass/air interfaces of a coverslip. The maximum intensity of the THG signals emitted from the cells were always one order of magnitude lower in comparison with the ones detected from the glass/air interface of the second coverslip, which was used to hold the sample.

THG intensity signal is strongly affected by the size of the sub-cellular structures and the resolution of the apparatus, specifically the numerical aperture of the objective and the condenser lenses. The described set-up and imaging conditions were employed in previous studies [8, 21] showing that lipid rich structures were the predominant sources for high THG signals obtained from various biological specimens (microglia cells, *Caenorhabditis elegans*).

The laser power on the sample plane was 40 mW for all measurements (~0.8 nJ per pulse). The described setup scans 500 × 500 pixels THG and TPEF image in one (1) second. To improve the signal to noise ratio (SNR), 20 scans were averaged for each final image. To further improve image quality, a series of 2D optical sections were obtained at 1 μm intervals ($z$ stack) and projected (maximum intensity projection) onto a single plane. Image J software was used for data viewing and processing (NIH, http://imagej.nih.gov/ij/).

## 2.3 THG quantification analysis

### 2.3.1 Signal's mean total area calculation

All samples were imaged under constant irradiation conditions (mean energy per pulse, linear polarization of the incident beam at the sample plane, dimensions of the scanning region, number of pixels, amplification of the PMT units). THG intensity values were collected from the photomultipliers' tubes (PMTs), stored in 2D 500 by 500 matrices and represented a single slice image of the sample. Image J software was used for image processing and thresholding. THG signal quantification was performed by setting a constant threshold in the obtained normalized 8-bit slice images, so that regions generating high levels of nonlinear signal were solely detected and isolated. The threshold was set to allow only 30% of the THG signal of the cell area to be analyzed and measured. The obtained calculated area corresponded to the cellular membrane, the nucleus membrane and the lipid droplets of each cell. During data calculations, whole (Figure 2 supplementary material) or compartmentalized cells (Figure 3 supplementary material), were investigated.

The quantification of mean THG area was calculated from the 10 central sequential z slices of each cell. Forty cells were tested for each case [8].

For cell compartmental quantification, cellular, nuclear membrane and intracellular signalling were isolated manually and measured using Image J software.

### 2.3.2 Signal's intensity calculation

For the quantification of the mean THG intensity, the values of a number of $N$ cells, were firstly normalized to a standard THG intensity value. Then the values were quantified by setting again a constant threshold, so that only the regions that provide high THG signals could be examined (mainly intra cellular lipid droplets, cellular and nucleus membranes). An algorithm designed and programmed in MATLAB environment was employed for the manual selection of representative cell areas of each slice and estimation of their mean pixel value. The integrated THG intensity over the total pixel area for each slice of a cell was calculated by multiplying the representative area with the mean intensity value of the corresponding pixels. The weighted mean pixel value of each cell was obtained by repeating this procedure for the 10 central slices of the sample.


© 2016 WILEY-VCH Verlag GmbH & Co. KGaA, Weinheim

### 2.4 FTIR spectra analysis

Cells were deposited on IR transparent KBr windows (approximately 20 µl with $10^4$–$10^5$ cells). FTIR experiments were carried out using a Bruker Vertex 70v spectrometer equipped with a KBr beamsplitter and a room temperature broad band triglycine sulfate (DTGS) detector in absorption mode. Interferograms were collected at 4 $cm^{-1}$ resolution (8 scans), apodized with a Blackman-Harris function, and Fourier transformed with two levels of zero filling in order to yield spectra encoded at 2 $cm^{-1}$ intervals. Before scanning, KBr background was recorded and each sample spectrum was obtained by automatic subtraction of the background. It has be noted that FTIR spectra values provided information for the slight changes of absorption of the cellular compartments and averaged over the entire cell area, so that FTIR measurements could be considered as cell size dependent.

The spectra were processed by using the software supplied by the instrument manufacturer (OPUS software package; Bruker Optics, Germany). The FTIR spectra along with their first and second derivative curves were used to highlight the components of different spectral regions and to determine the approximate values of the peak positions of the components. The integrated area of the recorded FTIR peaks and their second derivative were determined using OPUS software in order to estimate the concentration of the corresponding bonds.

### 2.5 Statistical analysis

For multi group comparisons, one-way analysis of variance (ANOVA) with a post hoc Tukey test was used. The level of significance was set at $p < 0.05$. Data were analyzed with SPSS 16.0 software.

## 3. Results

THG imaging provides unique structural, anatomical and morphological information in various biological samples at cellular and sub-cellular level. Previous studies have shown that THG imaging could distinguish between resting and activated microglia, where lipid bodies were shown to be the major signal emitting organelles [8]. Furthermore, infrared spectra demonstrate significant differences between cancer and control cells [22, 23]. Taking into consideration the activation state of cancer cells, the present work concentrated on breast cancer and inquired whether THG imaging and infrared spectra could distinguish between malignant and healthy cells.

### 3.1 Specific features of THG signalling in breast cancer cell line classification

Six different breast cancer cell lines, classified as luminal, HER2 positive and triple negative [24], were cultured and submitted to THG imaging. Each cell line presented a specific THG signalling pattern. Thus, luminal cell lines (MCF7 and T47D) showed both intracellular and membrane THG signal, HER2+ (BT474 and SKBR3) showed mainly intracellular signal, while triple negative (MDA-MB231

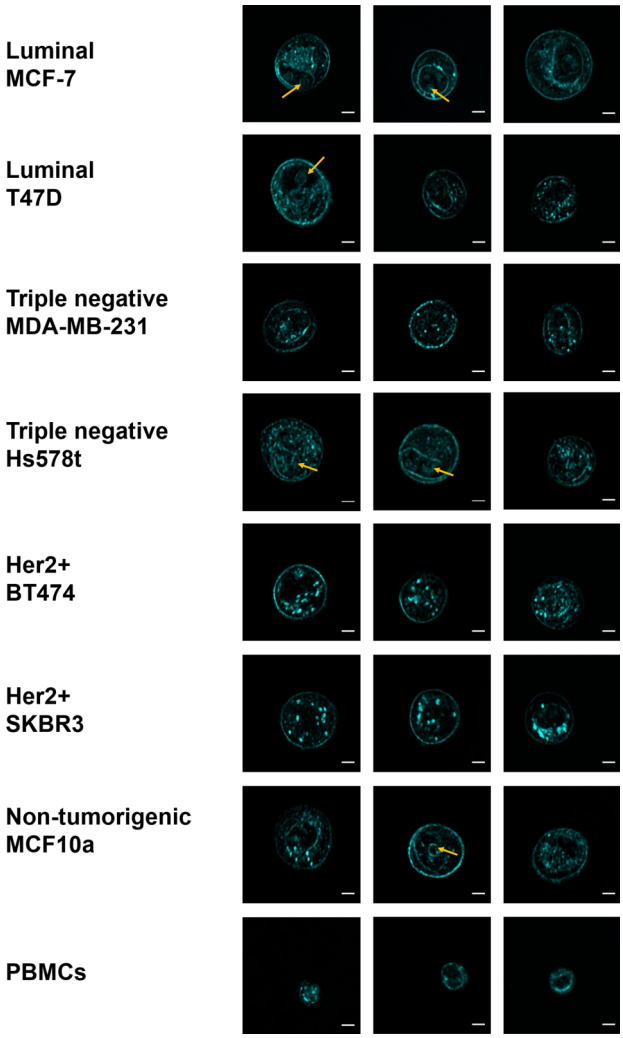


**Figure 1** THG images (*z*-projection) of breast cancer cell lines and control cells. Luminal (MCF7 and T47D), HER2 positive (BT474 and SKBR3), triple negative (MDA-MB231 and Hs578T) cancer cell lines as well as non-tumorigenic MCF10a breast cells and control PBMCs were submitted to THG imaging as described in Section 2.2. The yellow arrows depict the amorphous nucleus and the enclosed nucleolus of cells. Characteristic THG imaging from three different cells of the same cell type are presented for each case. Scale bar depicts 5 µm.

© 2016 WILEY-VCH Verlag GmbH & Co. KGaA, Weinheim

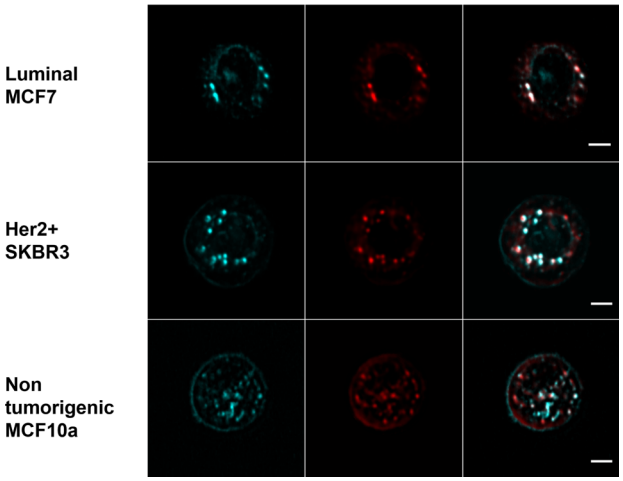


**Figure 2** 2D THG images of MCF-7, SKBR3 and MCF10a cells (cyan) and 2D TPEF images of the same cells stained with Nile-Red (red). In the merged images (third column), the co-localization of THG-TPEF signals is presented in white colour. The scale bar depicts 5 μm.

and Hs578T) cells showed mainly nuclear and cellular membrane signal. Non-tumorigenic MCF10a cells displayed both membrane and intracellular signal, while PBMCs displayed essentially intracellular THG signalling (Figure 1). In contrast to PBMCs, where nuclei were visualized as regular black areas in the cell due to the dense chromatin structure, cancer cells showed irregular nuclear shapes with enlarged nucleoli (Figure 1, arrows).

In order to evaluate the lipid droplet origin of the intracellular THG signal, the cells were stained with Nile red (lipid droplet staining) and THG and TPEF signals were recorded simultaneously (Figure 2). The multimodal merged images revealed significant co-localization of THG signal and lipid droplet staining, confirming that lipid droplets were the main subcellular structures generating high THG signals.

## *3.2 Quantification of THG signalling in breast cancer cell lines*

In an attempt to quantify the THG signalling, THG intensity values were collected, stored and processed using the Image J software (see Section 2.3). The mean total area (mean number of pixels above an intensity threshold) of THG values of PBMCs was significantly lower ($p < 0.05$) than those of cancer cells (Figure 3a), while both HER2-positive BT474 and SKBR3 breast cancer cells exhibited statistically significant higher values as compared to all other cells.

Taking into consideration the cell size (normalization by dividing the mean total area by the surface cell area of each cell type), HER2 positive cell lines, still demonstrated significantly increased levels of THG signal ($p < 0.05$; Figure 3b). These results indicated that THG signal quantification could distinguish HER2+ cells from the other types of breast cancer. However, one should not normalize the results as to cell area, because size is an important feature of cancerous *versus* physiological cells.

Dissecting THG signal quantification into the different cellular compartments, while maintaining the

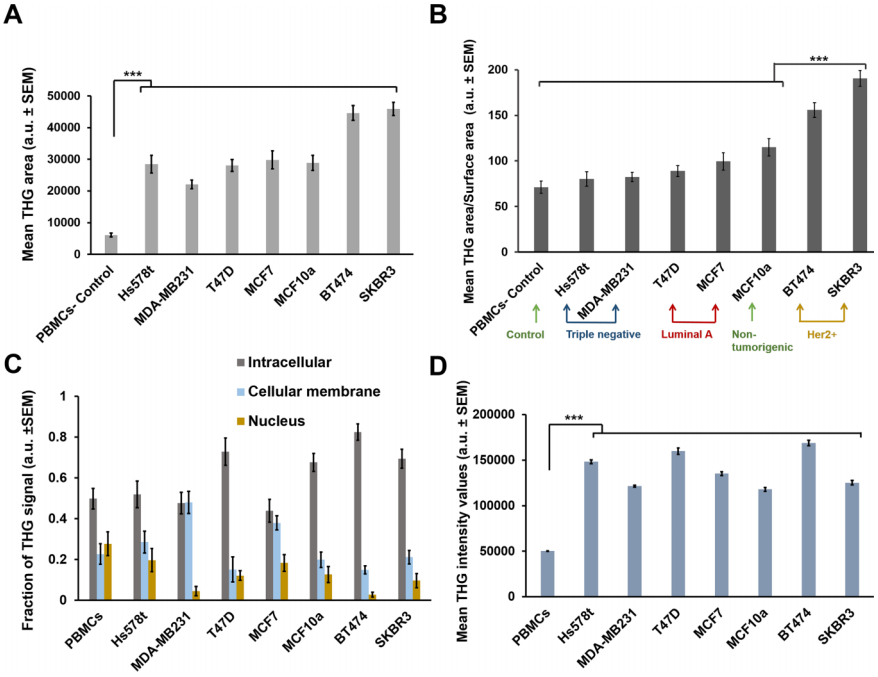


**Figure 3** THG signal quantification depicted as (**a**) mean total area, (**b**) mean THG area divided by the surface cell area. Surface cell area represents the image area enclosed by the signal of the outer cellular membrane. (**c**) THG area of the different cellular compartments (intracellular, cellular membrane, nucleus) divided by the total area of each cell and (**d**) Mean THG intensity. Data represent mean values ± S.E.M. ($n = 40$ each case). The *** denotes $p < 0.005$ statistical significance.


© 2016 WILEY-VCH Verlag GmbH & Co. KGaA, Weinheim

same threshold, there was an attempt to isolate the THG signal acquired from the cell surface membrane, the intracellular compartments as well as the nuclear membrane. Such quantification revealed that THG signal arose mostly from the intracellular area in BT474 cells and the cellular membrane in MDA-MB231 cells. In PBMCs, THG signal mostly originated from nuclear membranes, whereas in SKBR3 cells, THG signal was emitted by surface membrane, intracellular area as well as the nuclear membrane (Figure 3c).

Furthermore, THG intensity quantification showed that all cell lines tested, displayed significantly higher values as compared to PBMCs ($p < 0.005$, Figure 3d). The mean THG values represent the weighted mean values of the integrated intensity over the total pixel area of 10 central slices of the cell.

### *3.3 THG imaging correlation to FTIR spectra analysis*

Except from lipid bodies which have been considered to play an important role in the tumorigenic process, lipid rafts have also been shown to be involved in cell adhesion and migration of tumor cells [25]. To evaluate whether membrane acquired THG signal could correspond to lipid rafts, FTIR analysis was performed and correlated to THG signalling.

Focusing on MCF7, MDA-MB231, BT474 cells and PBMCs, FTIR spectra analysis could clearly distinguish between cancer cells and control PBMCs, which were always showing lower absorbance levels (Figure 4). However, except from the absorbance amplitude, the obtained FTIR spectra and the 1st derivative analysis could not reveal any specific wavelengths differentiating PBMCs from cancer cells.

Upon acquisition of 2nd derivative as described in Section 2.4, the calculation of the 2nd derivative mean area of FTIR spectra, unwrapped some significant differences. Among the absorption wavelengths the ones that correspond to cholesterol, phospholipids and C=O stretching modes mostly define lipid rafts [26]. Thus, focusing on wavelengths 1737 $cm^{-1}$ (lipids) [27, 28], 1746 $cm^{-1}$ (lipids) [29], 2845 $cm^{-1}$ (lipids, cholesterol/phospholipids) [19, 30], 2853–2858 $cm^{-1}$ (lipids) [19, 31] and 2910 $cm^{-1}$ (cholesterol/phospholipids) [30], it could be observed that BT474 cells displayed higher mean spectrum areas as compared to MCF7, MDA-MB231 cancer cells

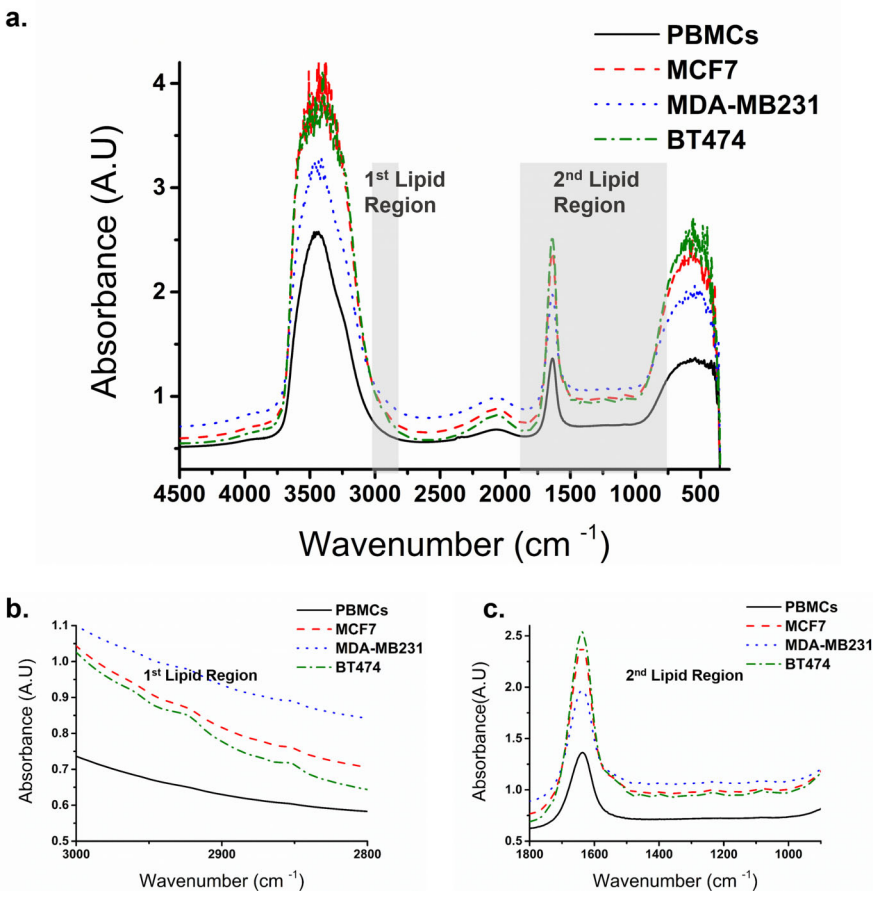


**Figure 4** (**a**) FTIR spectra of cancer cell lines (BT474, MCF7, MDA-MB231) and control cells (PBMCs) and their lipid regions (**b**) 2800–3000 $cm^{-1}$ and (**c**) 900–1800 $cm^{-1}$ respectively. One representative experiment out of three is shown here.

© 2016 WILEY-VCH Verlag GmbH & Co. KGaA, Weinheim

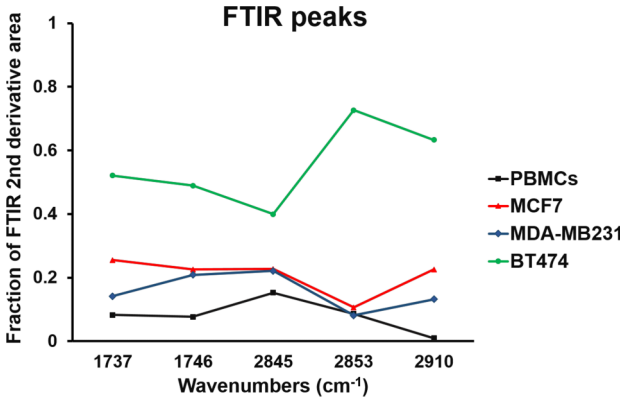


**Figure 5** Fractions of FTIR 2nd derivative spectrum area for the wavelengths 1737, 1746, 2845, 2853 and 2910 $cm^{-1}$ respectively. Fractions represent the calculated 2nd derivative area of each cell type divided by the sum of the 2nd derivative area of all cells for each characteristic peak. Data represents mean values of three independent experiments for the five different peaks, which mainly correspond to lipid rafts. BT474 cells appear higher values as compared to MCF7, MDA-MB231 breast cancer cells and PBMCs. SEM is in the order of 25% of the values (not shown) due to the limited number of FTIR measurements ($n = 3$ in each case).

and PBMCs (Figure 5). These results correlated to the mean THG area divided by the surface cell area ($R^2_{1737} = 0.9958$, $R^2_{1746} = 0.9592$, $R^2_{2845} = 0.9675$, $R^2_{2853} = 0.9198$, $R^2_{2845} = 0.9954$, Figure 6$a_1$, $a_2$, $a_3$, $a_4$, $a_5$) and to mean THG intensity values ($R^2_{1737} = 0.7264$, $R^2_{1746} = 0.8017$, $R^2_{2845} = 0.7436$, $R^2_{2910} = 0.8922$, Figure 6$b_1$, $b_2$, $b_3$, $b_5$). With exception of the mean THG intensity at 2853 $cm^{-1}$ ($R^2_{2853} = 0.4474$, Figure 6$b_4$), in all other cases, satisfactory fitting values were obtained.

## 4. Discussion and conclusion

Nonlinear optical imaging techniques shed new light in the delineation of various biological and biomedical processes while providing a strong impact on early detection of diseases [8, 9, 32–36]. In this study, THG microscopy was used as a new, label free, non-destructive imaging technique for the classification of different subtypes of breast cancer cell lines and their distinction from non-cancer cells. The discrimination between the different types of cells was based on the quantification of collected THG signals and their correlation to FTIR spectra. It was observed that breast cancer cells displayed an increased lipid content compared to normal cells, which correlated to FTIR 2nd derivative mean spectra area of cholesterol/spingomyelin rich areas that possibly correspond to lipid rafts.

Previous studies had shown that THG imaging could distinguish between activated and non-activated microglia cells [8]. Breast cancer cell lines, which are expected to display a constantly metabolically activated profile, were shown to provide higher levels of THG signal in terms of both intensity and mean signal area, as compared to controls. In this study, PBMCs from healthy blood donors and the breast epithelial MCF10a cell line were used as controls. However, none of these two cell types can readily be considered as control of the malignant cancer cells. PBMCs have a different cell origin, while MCF10a, which represent non-tumorigenic breast epithelial cells, have been isolated from a Caucasian female with fibrocystic disease. Therefore, these cells were only used as benchmarks for comparison reasons. Interestingly, depending on the cell type studied, THG signal was not evenly distributed in the cells, localized either at the level of membranes and/or specific cytoplasmic structures. Thus, luminal type cell lines, characterized by the expression of estrogen and/or progesterone receptors and represented by MCF7 and T4TD cells showed intracellular and membrane THG signal. The HER2 positive breast cancer cells, characterized by HER2 expression and represented by BT474 and SKBR3 cell lines showed mainly intracellular THG signal, while the triple negative cell lines, MDA-MB-231 and Hs5787, showed mainly nuclear and cellular membrane signal.

The cytoplasmic structures were demonstrated to co-localize with LDs, which is in agreement with previous observations [8, 12, 15, 37]. Indeed, increased numbers of LDs have been correlated to various pathologic conditions. Thus, increased cytoplasmic lipid accumulation in leukocytes and other cells has been observed in a number of clinical and experimental inflammatory and infectious diseases [13, 38–40].

Membrane signalling was specifically observed in the most aggressive MDA-MB-231 and Hs5787 cells. Indeed, previous studies have indicated that membranes play a crucial role in tumor cell dissemination and metastasis [41–43]. Similarly to the cell membrane, nuclear envelope also consists of a lipid bilayer and it has been shown that alterations in the nuclear membrane affect the behaviour and phenotype of tumor cells [44]. Membrane constitution has been considered to play an important role in breast cancer cell function. During cell activation, microdomains to the cell membrane cluster together proteins and specific lipids involved in the regulation of various cellular processes, many of which are altered in cancer cells. In addition, lipid rafts are influenced by nutrition [45]. It has been shown that fatty acid supplementation sensitises human mammary tumor cells to the cytotoxic effects of anti-cancer agents [46]. Thus, lipid rafts have been considered to have a role


© 2016 WILEY-VCH Verlag GmbH & Co. KGaA, Weinheim

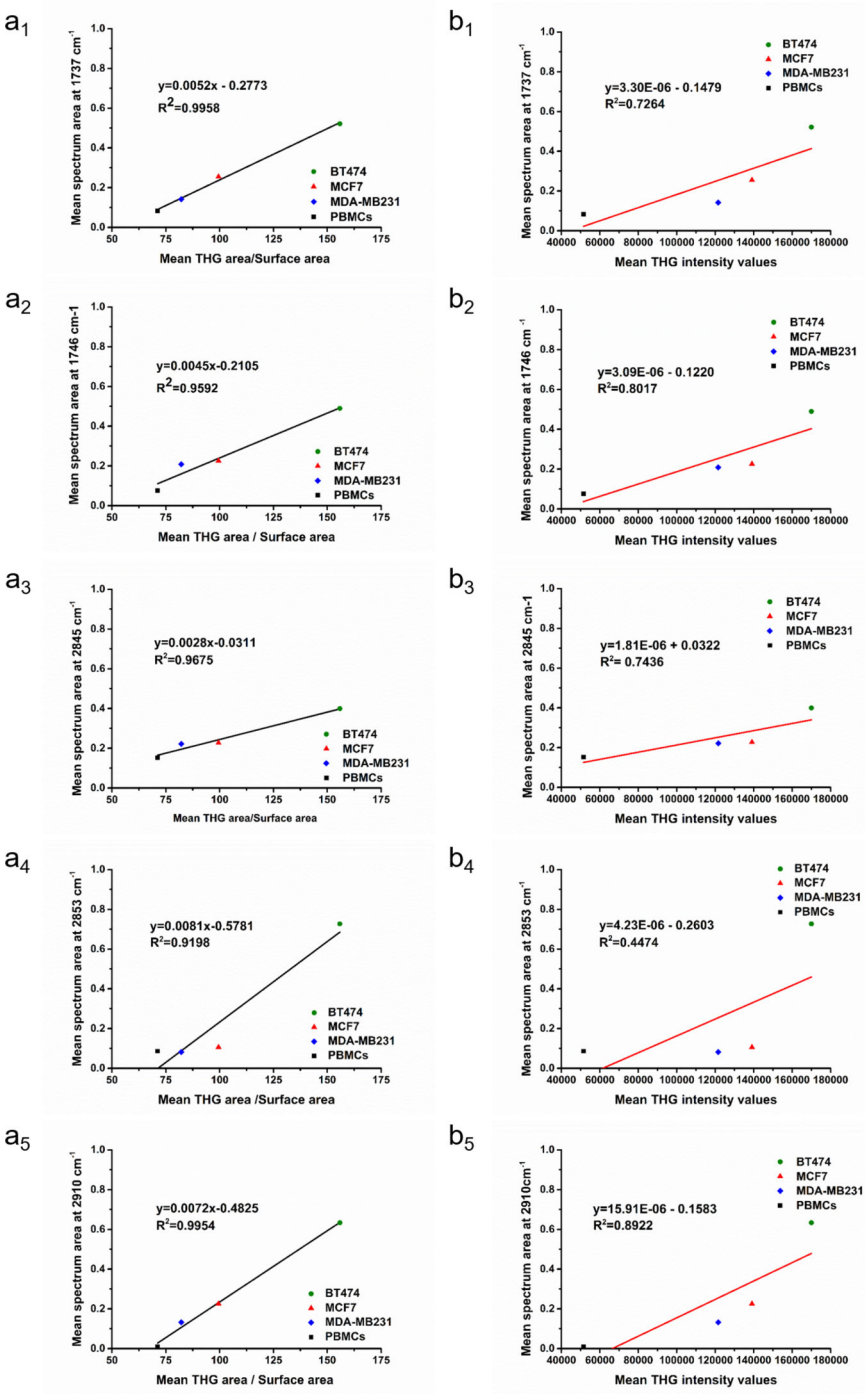


**Figure 6** Correlation of FTIR 2nd derivative spectra with THG (**a**, left column) mean area divided by the surface cell area and (**b**, right column) mean THG intensity values for specific peaks of spectrum of lipid regions.

in cancer initiation, progression and cell migration [47].

Quantification of the THG signal in the different sub-cellular regions demonstrated that BT474 cells mostly displayed intracellular localization of the signal, while in MDA-MB231 cells the cellular membrane was the major source of THG signal. In normal PBMCs, signal mostly originated from nuclear membranes, whereas SKBR3 cells displayed surface membrane, intracellular area and nuclear membrane staining.

Additional information as to the breast cancer cells studied here was provided by the nuclear shape. In THG imaging, nucleus is generally presented as a black area in the cell, due to the dense chromatin structure, which does not allow the nonlinear light scattering. All cancer cells studied here were characterized by irregular size and shape, en-

© 2016 WILEY-VCH Verlag GmbH & Co. KGaA, Weinheim

larged nucleus and nucleolus, which are in agreement with previous studies [48–52].

In an attempt to correlate THG signalling to chemistry, one cell line from each breast cancer subtype was submitted to FTIR analysis. Although each cell line showed a specific FTIR spectrum, specific spectra present in cancer cells only, could not be detected. Concentrating on spectra characterizing cholesterol/sphingomyelin rich regions, as a simulation to lipid rafts, it was shown that the mean area of 2nd derivative spectra correlated with THG signal mean area and intensity. Therefore, the results presented here showed for the first time a correlation between THG imaging and FTIR analysis, relating thus THG imaging to chemistry. Although Coherent Anti – stokes Raman Scattering (CARS) microscopy has been proposed as a promising tool in chemical imaging, this technique requires more complex laser systems [53–55].

Correlating THG imaging to organelle chemistry would be a quite important feature to the analysis of biological samples. Since THG signal is generated from the refractive index changes and dispersion, it can be hypothesized that chemical changes to the membranes could affect THG signalling. Indeed, aromatic hydrocarbons cause dilation of the intracellular space, altering thus intra-cytoplasmic vacuoles [56]. The correlation of THG signal area and intensity to C–H, C=O stretching, cholesterol and phospholipid spectra indicates that THG signal could reflect the presence of aromatic hydrocarbons and cholesterol. In addition, cholesterol and the carbonyl group of sphingomyelin is obscured by the complexity of different possible hydrogen bonding and coupling between the N–H and the C=O group vibrations, apparent in lipid rafts [26]. Thus, the increased THG signal observed in activated cells could be extrapolated to increased lipid raft content of the membranes. Further studies using artificial membranes with variable hydrocarbon, shingomyelin and cholesterol constitution are needed to definitely demonstrate such correlation.

In conclusion, THG microscopy can discriminate between breast cancer cells of different subtypes and could be used for the label-free detection of breast cancer cells among PBMCs (Figure 4 supplementary material). Thus, quantification of the THG signal provides an objective classification pattern. The correlation of THG signalling to chemistry could open new areas of research and technology, where fast label free imaging could provide valuable information on the malignant area of the cells or tissues.

The presented work has a significant clinical potential, since it perceives quantitative changes in healthy and malignant human cells. Understanding the intracellular lipid droplet distribution and membrane morphology could provide information on lipid metabolism in tumour cells for exploitation as therapeutic targets [13–16]. Although more research is needed to understand the correlation between lipids and cancer pathology and automate the segmentation analysis, the nonlinear imaging modality of THG has the potential to discriminate among the different cancer cell types [9]. THG microscopy assesses lipid and membrane changes in healthy, cancer cells and tissues ex vivo by absolute parameters that quantify inflammatory damage. This paves the way for novel, label free methods to quantify therapeutic response in cancer and computerize histological examinations in terms of digital pathology. Finally, the development of an "imaging pen" that will quickly analyze human tissues for disease and infection and help surgeons to determine cancer limits during surgery is within the future goals of our laboratories.

## Supporting Information

**Supplement Figure 1.** Experimental apparatus of the nonlinear microscope. GM galvanometric mirrors, L, L1,L2 lenses, M mirrors, DM dichroic mirror, PMT1,2 photomultiplier tubes, fs femtosecond laser

**Supplement Figure 2.** Quantification of THG signals using thresholded images: (a) $z$ projection THG image of a cancer cell and (b) its thresholded image respectively. Scale bar depicts 5 μm.

**Supplement Figure 3.** $z$ projection THG images of cancer cell's parts (a) whole cell (b) cellular membrane (c) nucleus area and (d) intracellular area. Lower their thresholded images are shown respectively. Scale bar depicts 5 μm.

**Supplement Figure 4.** 3D graph for the distinction between cancer and PBMCs cells via THG signals quantification. THG area/ surface area of the cell in $x$-axis, THG intensity values in $y$-axis and cell surface area in $z$-axis. The Her2 positive cancer cells (BT474 and SKBR3) and the PBMCs normal cells appeared clearly as separable sub populations of spots in the scatter plot ($N = 20$ for each cell type).

**Acknowledgements** This work was financial supported by the European project "LASERLAB-EUROPE IV – BIOAPP" (GA 654148). Author G.K. acknowledges the ERA.Net RUS Plus project EXODIAGNOS (under the EU FP7 grant agreement no 609556).

## References

[1] T. Meyer, M. Schmitt, B. Dietzek, and J. Popp, Journal of biophotonics **6**, 887–904 (2013).



© 2016 WILEY-VCH Verlag GmbH & Co. KGaA, Weinheim

[2] W. R. Zipfel, R. M. Williams, and W. W. Webb, Nat Biotech., **21**, 1369–1377 (2003).
[3] G. J. Tserevelakis, S. Psycharakis, B. Resan, F. Brunner, E. Gavgiotaki, K. Weingarten, and G. Filippidis Journal of biophotonics **5**, 200–207 (2012).
[4] C. Kyvelidou, G. J. Tserevelakis, G. Filippidis, A. Ranella, A. Kleovoulou, C. Fotakis, and I. Athanassakis, J Struct Biol. **176**, 379–386 (2011).
[5] C. F. Chang, C. H. Yu, and C. K. Sun, Journal of biophotonics. **3**, 678685 (2010).
[6] N. Olivier, M. A. Luengo-Oroz, L. Duloquin, E. Faure, T. Savy, I. Veilleux, X. Solinas, D. Débarre, P. Bourgine, A. Santos, N. Peyriéras, and E. Beaurepaire, Science **329**, 967–971 (2010).
[7] C.-K. Tsai, Y.-S. Chen, P.-C. Wu, T.-Y. Hsieh, H.-W. Liu, C.-Y. Yeh, W.-L. Lin, J.-S. Chia, and T.-M. Liu, Biomedical Optics Express **3**, 2234–2243 (2012).
[8] E. Gavgiotaki, G. Filippidis, M. Kalognomou, A. A. Tsouko, I. Skordos, C. Fotakis, and I. Athanassakis, Journal of Structural Biology. **189**, 105–113 (2015).
[9] N. V. Kuzmin, P. Wesseling, P. C. Hamer, D. P. Noske, G. D. Galgano, H. D. Mansvelder, J. C. Baayen, and M. L. Groot, Biomed Opt Express **7**, 188-–1904 (2016).
[10] Y. Barad, H. Eisenberg, M. Horowitz, and Y. Silberberg, Applied Physics Letters **70**, 922–924 (1997).
[11] J. Squier, and M. Müller, Review of Scientific Instruments **72**, 2855–2867 (2001).
[12] D. Debarre, W. Supatto, A. M. Pena, A. Fabre, T. Tordjmann, L. Combettes, M. C. Schanne-Klein, and E. Beaurepaire, Nature methods **3**, 47–53 (2006).
[13] T. C. Walther, and R. V. Farese, Annual review of biochemistry **81**, 687–714 (2012).
[14] S. Martin and R. G. Parton, Nat Rev Mol Cell Biol. **7**, 373–378 (2006).
[15] M. Digel, R. Ehehalt, and J. Füllekrug, FEBS Letters **584**, 2168–2175 (2010).
[16] Y. Guo, K. R. Cordes, R. V. Farese, Jr., and T. C. Walther, J Cell Sci. **122**, 749–752 (2009).
[17] A. Derenne, O. Vandersleyen, and E. Goormaghtigh, Biochimica et biophysica acta **1841**, 1200–1209 (2014).
[18] Z. Movasaghi, S. Rehman, and D. I. ur Rehman, Applied Spectroscopy Reviews, **43**, 134–179 (2008).
[19] G. I. Dovbeshko, N. Y. Gridina, E. B. Kruglova, and O. P. Pashchuk, Talanta, **53**, 233–246 (2000).
[20] A. Jemal, F. Bray, M. M. Center, J. Ferlay, E. Ward, and D. Forman, CA: A Cancer Journal for Clinicians **61**, 69–90 (2011).
[21] G. J. Tserevelakis, E. V. Megalou, G. Filippidis, B. Petanidou, C. Fotakis, and N. Tavernarakis, PLoS ONE **9**, e84431 (2014).
[22] E. Farhadi, F. Kobarfard, and F. H. Shirazi, Iranian Journal of Pharmaceutical Research **15**, 213–220 (2016).
[23] J. Pijanka, G. D. Sockalingum, A. Kohler, Y. Yang, F. Draux, G. Parkes, K.-P. Lam, D. Collins, P. Dumas, C. Sandt, D. G. van Pittius, G. Douce, M. Manfait, V. Untereiner, and J. Sule-Suso, Lab Invest. **90**, 797–807 (2010).
[24] R. M. Neve, K. Chin, J. Fridlyand, J. Yeh, F. L. Baehner, T. Fevr, L. Clark, N. Bayani, J. P. Coppe, F. Tong, T. Speed, P. T. Spellman, S. DeVries, A. Lapuk, N. J. Wang, W. L. Kuo, J. L. Stilwell, D. Pinkel, D. G. Albertson, F. M. Waldman, F. McCormick, R. B. Dickson, M. D. Johnson, M. Lippman, S. Ethier, A. Gazdar, and J. W. Gray, Cancer cell **10**, 515–527 (2006).
[25] T. Murai, International journal of cell biology **2012**, 763283 (2012).
[26] Z. Arsov and L. Quaroni, Biochimica et Biophysica Acta (BBA) – Biomembranes **1778**, 880–889 (2008).
[27] H. Fabian, M. Jackson, L. Murphy, P. H. Watson, I. Fichtner, and H. H. Mantsch, Biospectroscopy **1**, 37–45 (1995).
[28] S. Yoshida, M. Miyazaki, K. Sakai, M. Takeshita, S. Yuasa, A. Sato, T. Kobayashi, S. Watanabe, and H. Okuyama, Biospectroscopy **3**, 281–290 (1997).
[29] G. Shetty, C. Kendall, N. Shepherd, N. Stone, and H. Barr, British Journal of Cancer **94**, 1460–1464 (2006).
[30] M. Huleihel, A. Salman, V. Erukhimovitch, J. Ramesh, Z. Hammody, and S. Mordechai, Journal of Biochemical and Biophysical Methods **50**, 111–121 (2002).
[31] M. F. K. Fung, M. K. Senterman, N. Z. Mikhael, S. Lacelle, and P. T. T. Wong, Biospectroscopy **2**, 155–165 (1996).
[32] J. Adur, V. B. Pelegati, A. A. de Thomaz, L. D'Souza-Li, C. Assuncao Mdo, F. Bottcher-Luiz, L. A. Andrade, and C. L. Cesar, J Biomed Opt. **17**, 081407 (2012).
[33] G. Thomas, J. van Voskuilen, H. C. Gerritsen, and H. J. C. M. Sterenborg, Journal of Photochemistry and Photobiology B: Biology **141**, 128–138 (2014).
[34] C. K. Chen and T. M. Liu, Biomed Opt Express **3**, 2860–2865 (2012).
[35] S. W. Chu, S. Y. Chen, T. H. Tsai, T. M. Liu, C. Y. Lin, H. J. Tsai, and C. K. Sun, Optics express **11**, 3093–3099 (2003).
[36] P. C. Wu, T. Y. Hsieh, Z. U. Tsai, and T. M. Liu, Scientific reports **5**, 8879 (2015).
[37] K. Yen, T. T. Le, A. Bansal, S. D. Narasimhan, J.-X. Cheng, and H. A. Tissenbaum, PLoS ONE **5**, e12810 (2010).
[38] P. T. Bozza and J. P. Viola, Prostaglandins, leukotrienes, and essential fatty acids **82**, 243–250 (2010).
[39] H. Abramczyk, J. Surmacki, M. Kopec, A. K. Olejnik, K. Lubecka-Pietruszewska, and K. Fabianowska-Majewska, Analyst **140**, 2224–2235 (2015).
[40] J. V. Swinnen, K. Brusselmans, and G. Verhoeven, Current opinion in clinical nutrition and metabolic care **9**, 358–365 (2006).
[41] M. He, S. Guo, and Z. Li, Scientific reports **5**, 11298 (2015).
[42] I. Dobrzyńska, B. Szachowicz-Petelska, B. Darewicz, and Z. A. Figaszewski, The Journal of Membrane Biology **248**, 301–307 (2015).
[43] H. Yamaguchi, Y. Takeo, S. Yoshida, Z. Kouchi, Y. Nakamura, and K. Fukami, Cancer Research **69**, 8594–8602 (2009).
[44] K. H. Chow, R. E. Factor, and K. S. Ullman, Nat Rev Cancer **12**, 196–209 (2012).

© 2016 WILEY-VCH Verlag GmbH & Co. KGaA, Weinheim

[45] P. Yaqoob, Annual Review of Nutrition **29**, 257–282 (2009).
[46] S. Colas, K. Mahéo, F. Denis, C. Goupille, C. Hoinard, P. Champeroux, F. Tranquart, and P. Bougnoux, Clinical Cancer Research **12**, 5879–5886 (2006).
[47] I. S. Babina, S. Donatello, I. R. Nabi, and A. M. Hopkins, Lipid rafts as master regulators of breast cancer cell function. Breast Cancer – Carcinogenesis, Cell Growth and Signalling Pathways, Book edited by G. Gunduz and E. Gunduz, In Tech. **92**, 287–295 (2011).
[48] R. Chiotaki, H. Polioudaki, and P. A. Theodoropoulos, Biochemistry and cell biology **92**, 287–295 (2014).
[49] M. Webster, K. L. Witkin, and O. Cohen-Fix, J Cell Sci. **122**, 1477–1486 (2009).
[50] J. Lin, W. Zheng, Z. Wang, and Z. Huang, Applied Physics Letters **105**, 103705 (2014).
[51] W. H. Wolberg, W. N. Street, and O. L. Mangasarian, Clinical cancer research: an official journal of the American Association for Cancer Research **5**, 3542–3548 (1999).
[52] D. Zink, A. H. Fischer, and J. A. Nickerson, Nat Rev Cancer **4**, 677–687 (2004).
[53] H. A. Rinia, K. N. J. Burger, M. Bonn, and M. Müller Biophysical Journal **95**, 4908–4914 (2008).
[54] C. L. Evans and X. S. Xie, Annual Review of Analytical Chemistry **1**, 883–909 (2008).
[55] C. Di Napoli, F. Masia, I. Pope, C. Otto, W. Langbein, and P. Borri, Journal of biophotonics **7**, 68–76 (2014).
[56] R. Meiß, U. Heinrich, H. Robenek, and H. Themann, Agents and Actions **12**, 254–257 (1982).


© 2016 WILEY-VCH Verlag GmbH & Co. KGaA, Weinheim